ETH Library

Millimeter-wave to near-terahertz sensors based on reversible insulator-to-metal transition in VO2

Journal Article

Author(s):
Qaderi, Fatemeh; Rosca, Teodor; Burla, Maurizio; Leuthold, Juerg; Flandre, Denis; Ionescu, Adrian M.

Publication date:
2023

Permanent link:
https://doi.org/10.3929/ethz-b-000615035

Rights / license:
Creative Commons Attribution 4.0 International

Originally published in:
Communications Materials 4(1), https://doi.org/10.1038/s43246-023-00350-x

This page was generated automatically upon download from the ETH Zurich Research Collection.
For more information, please consult the Terms of use.

communications
materials

ARTICLE

https://doi.org/10.1038/s43246-023-00350-x OPEN

Millimeter-wave to near-terahertz sensors based on reversible insulator-to-metal transition in VO_2

Fatemeh Qaderi[1✉], Teodor Rosca[1], Maurizio Burla[2], Juerg Leuthold[2], Denis Flandre[3] & Adrian M. Ionescu[1✉]

In the quest for low power bio-inspired spiking sensors, functional oxides like vanadium dioxide are expected to enable future energy efficient sensing. Here, we report uncooled millimeter-wave spiking detectors based on the sensitivity of insulator-to-metal transition threshold voltage to the incident wave. The detection concept is demonstrated through actuation of biased VO_2 switches encapsulated in a pair of coupled antennas by interrupting coplanar waveguides for broadband measurements, on silicon substrates. Ultimately, we propose an electromagnetic-wave-sensitive voltage-controlled spike generator based on VO_2 switches in an astable spiking circuit. The fabricated sensors show responsivities of around 66.3 $MHz.W^{-1}$ at 1 μW, with a low noise equivalent power of 5 $nW.Hz^{-0.5}$ at room temperature, for a footprint of 2.5×10^{-5} mm^2. The responsivity in static characterizations is 76 $kV.W^{-1}$. Based on experimental statistical data measured on robust fabricated devices, we discuss stochastic behavior and noise limits of VO_2 -based spiking sensors applicable for wave power sensing in mm-wave and sub-terahertz range.

[1]Nanoelectronic devices laboratory (Nanolab), Department of Electrical Engineering, École polytechnique fédérale de Lausanne (EPFL), EPFL STI IEL NANOLAB, ELB 335, Station 11, Lausanne 1015, Switzerland. [2]Institute of Electromagnetic Fields (IEF), Eidgenössische Technische Hochschule Zürich (ETHZ), ETZ K 82, Gloriastrasse 35, Zürich 8092, Switzerland. [3]ICTEAM, Ecole Polytechnique de Louvain (UCLouvain), ELEN, Place du Levant 3/L5.03.02, Louvain-la-Neuve 1348, Belgium. ✉email: fatemeh.qaderi.92@gmail.com; adrian.ionescu@epfl.ch

Vanadium dioxide (VO_2) is a transition metal oxide with correlated electrons which undergoes a first-order insulator-to-metal transition (IMT) at 340 K from a low-temperature monoclinic insulating state to a high-temperature rutile metallic state, accompanied by structural, electrical, and optical changes[1,2]. The potential of IMT along with its sensitivity to external stimuli makes it promising for a variety of applications in resistive memories[3–5], optical switches[6,7], sensors[8–10], tunable photonic devices[11,12], brain-inspired and neuromorphic architectures[13–15]. Moreover, RF/MW applications of tunable structures are reported based on various types of VO_2 layers[16,17]. We target the sensor application in the frequency range of mm-wave and terahertz (THz). THz detectors are widely growing in different applications in spectroscopy[18], astronomy[19], biomedicine[20], imaging[21], surveillance security[22], high-data-rate communication[23], etc.

Aside from thermal stimuli, the phase transition can be triggered by other perturbations, such as optical pumping or changes in electric field, pressure, and doping. The mechanism of electric-field-driven IMT has been under debate for a long time. Formation of conducting filaments at bias voltages above a threshold is explained in some studies[24], while the mechanism of filamentation has been differently interpreted, such as the non-uniform current distribution followed by local Joule heating[24–26], or a breakdown mechanism similar to the one in thin oxides[27]. On the other hand, it has been discussed that the electric field can induce IMT through nucleation of conducting filaments similar to the mechanism in chalcogenide-based phase-change memory and switches[28] or without the need for a thermal process in Mott insulators[29–31]. The physics of such transitions is still under debate but it is recognized that it involves nucleation processes related to conductive path formation that are stochastic in nature[32].

Resistive switching in VO_2 based on electric-field-assisted carrier generation, which leads to critical doping levels making the Mott insulator unstable, allows moderate fields to excite a large number of carriers with negligible heating[33]. The idea of electric-field-driven carrier generation is also reinforced by localized triggering of IMT by means of carbon nanotube (CNT)s to enhance the electric field locally and decreasing the required voltage for IMT in VO_2 thin films[34]. Also, the feasibility of ultrafast VO_2 switching into a metastable metallic state[35] indicates a tunneling mechanism, in which long-lived metallic domains are generated by intense multi-terahertz excitation. The idea of above-thermal-process speed is also reinforced by THz spectroscopy of the ultrafast photoinduced IMT in VO_2[36].

Considering the thermal requirements for transition between insulating (M_1) and metallic (R) crystal phases ($2.32\,eV/nm^3$) calculated by integrating heat capacity and latent heat[2], the fundamental process of photoinduced phase transition turns out to show a different mechanism from a complete thermally induced transition, and ultimately a density-driven mechanism is suggested for this transition[37]. This is essentially practical in the case of THz and mm-wave, as they cannot actuate carriers through the band-gap in a semiconductor. A first demonstration of field-induced IMT of VO2 was reported using picosecond THz waveforms[38].

Among room temperature technologies for millimeter-wave (mm-wave)/ THz detection, one can consider field effect transistor (FET) detectors[39–47], Graphene or 2D material-based structures[48–55], diodes and rectifiers[56–58], photoconductive detectors[59,60], and bolometers[61,62]. The sensing mechanism in FET detectors is generally through the direct voltage induced in the channel according to the plasma waves[63]. 2D material-based transistors and switches mostly detect based on the transfer function of the channel which is activated by radiation[52]. Photoconductive materials are used in detectors according to their photo-responsivity (activation of the carriers by exposure)[60]. Diodes and rectifiers have a big role in THz detection for their nonlinearity-based, fast response. The two latter mechanisms are also used in heterodyne systems. Bolometers range from different materials which show a temperature coefficient of resistivity (TCR), and, particularly because VO_2 has a considerable TCR, it is worth comparing the VO_2-based detectors with our device. We have summarized most of the above detectors compared with our proposed one in terms of responsivity, noise, and speed in the discussion section.

There are specific challenges in detection mechanisms based on VO_2 thermal response such as VO_x micro-bolometers, which use TCR in these materials[64,65]. Experimental VO_2-based bolometers[66–69] have reported the operation by exploiting the semiconductor phase of VO_2, i.e., at room temperature or normal temperatures well below the phase change (where $TCR_{normal} = 2–6\%K^{-1}$[69]). The cliff of the transition is not used experimentally, however, there are simulation[65] and modeling works[70,71] assuming TCR_{max} upto $171\%K^{-1}$[65]. Moreover, according to the experimental data of the transition edge bolometer in[66], operating in the hysteresis region does not lead to any expected higher responsivity, but even half of the one when operated at TCR_{normal} in periodic acquisition mode, due to formation of minor hysteresis loops and the loop accommodation process[66]. The high-resistance VO_2 does not have a noticeable absorption of THz at the operating temperature of these bolometers[72]. This motivates the common use of THz absorbers for THz sensing by bolometers.

In our method, instead of using the slope of resistance, we monitor the location of the cliff and its displacements due to the incoming signal. The modulation of this transition with the signal is converted into a variation of the oscillation frequency as our detection scheme is a VO_2-based stochastic oscillator. The observed IMT voltage modulation was interpreted as field-induced enhancement of carrier density (Poole–Frenkel effect) succeeded by Joule heating due to electron-lattice coupling, which then stabilizes the metallic phase. For transition edge VO_2 bolometers, the lattice instabilities close to the phase-change temperature along with the local Joule heating can interfere with the bias control, as well as confining the dynamic range of the input[71,73]. In the device configuration of our work we are no more confronted by such instabilities and the power range can go broader (over a milli-watt) compared to that of bolometers (up to 20 μW[64]).

We design and experimentally demonstrate a stochastic power sensor by investigating the interaction of mm-wave and VO_2 at a controlled ambient under small DC voltage bias (below 2.5 V) at room temperature. The responsivity is at least three times larger than the similar sensors[74], along with a limit of detection (LoD) comparable to the state of the art[75], and a footprint of one order of magnitude smaller than the typical of VO_2 sensors[74].

We report on the stochastic behavior of switching based on experimental statistical data measured on robust fabricated VO_2 devices, using a spike oscillator readout. We harness the stochasticity, which translate in Poisson noise challenges. In order to study VO_2 electrical properties and the material interaction with the electromagnetic wave within a broadband of mm-wave range, we conduct 2-port experiments on a coplanar waveguide (CPW) interrupted by a VO_2 device in the signal line. The experiments are generally based on the actuation of VO_2 by mm-wave, assisted by a collective effect of a bias voltage. Using a pair of coupled antennas, one as the emitter and the other as the receiver, we establish the wireless short-range detection concept in mm-wave range. The receiving antenna has been designed and fabricated with VO_2 encapsulated in the area where it concentrates the incoming wave.

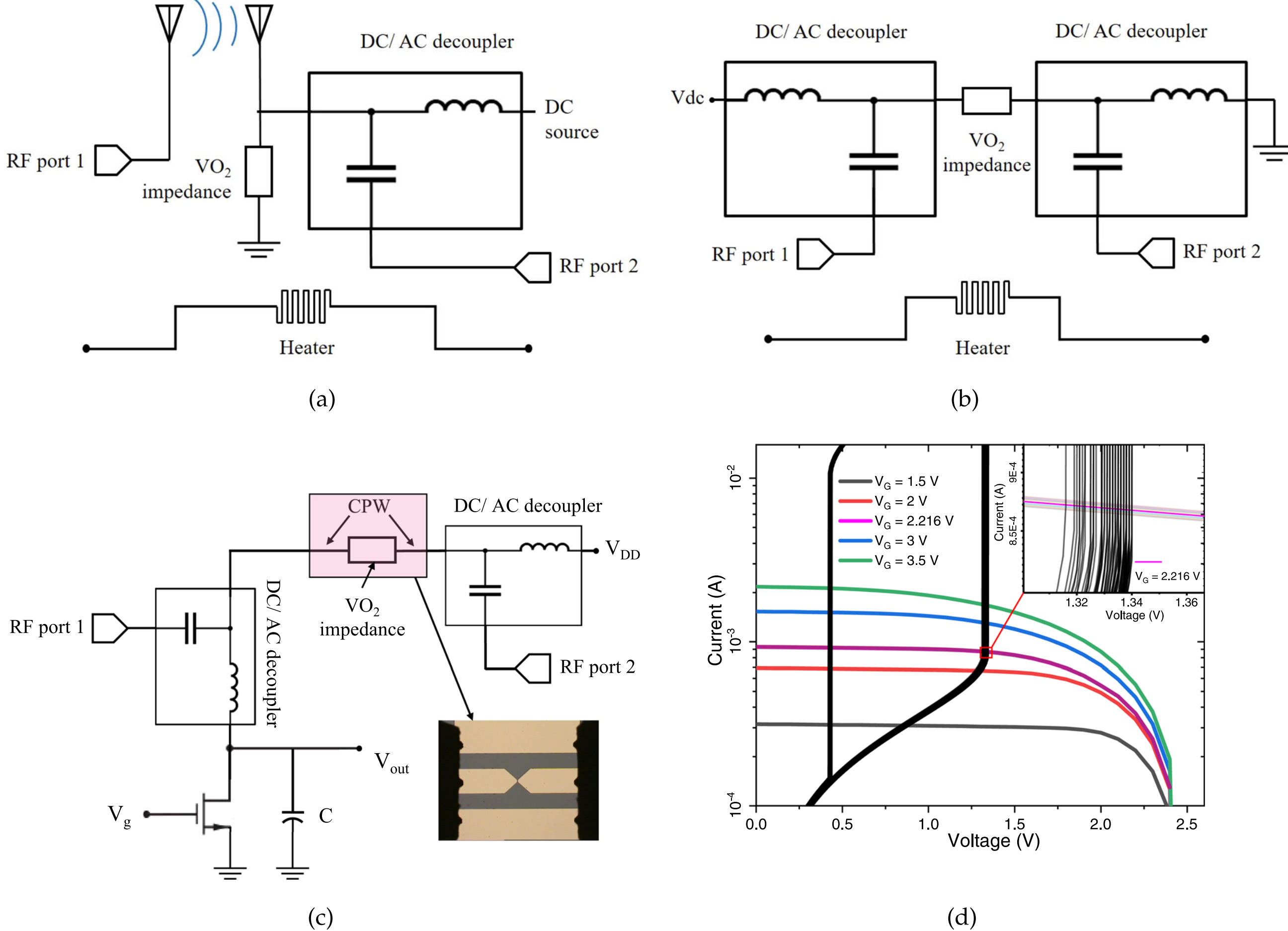

Fig. 1 Mm-wave detection method and the experimental setup. a VO_2 in coupled antennas case, **b** VO_2 in interrupted CPW case, **c** astable circuit using a 2-terminal VO_2 device in interrupted CPW in series with a MOSFET, **d** the initial operation point of the oscillating sensor is set by the intersection of the static characteristics of VO_2 (V_{VO_2})and the series drain-source voltage of the NMOS transistor ($V_{DD} - V_{ds}$) at specific points supporting astability. Inset: the operational bias points and multiple cycles of experiments suggesting non-deterministic behavior.

According to the available facilities the antennas are designed for mm-wave frequency range, while further scaling the antennas design (which is feasible through the same fabrication process for dimensions down to 1 µm) can shift the operational frequency up to THz. In terms of the detection mechanism, the material shows responsivity to a wide range of input frequencies from RF to THz, infrared (IR), visible, and UV[76–78]. Ultimately, we propose a readout circuit by means of an astable multivibrator formed of a VO_2 impedance in series with an NMOS transistor (Fig. 1c), in which the change in the frequency of oscillations represents the power applied to the VO_2 sensor.

Results

Principles of detection using VO_2 IMT threshold voltage shifting. It is recognized that different excitation sources applied simultaneously can create a collective effect to assist the phase transition in correlated oxides such as VO_2. According to the measured static current-voltage characteristics of VO_2 2-terminal switches, the IMT threshold voltage shows a decline at elevated temperatures[79]. This gives the inspiration of combining a DC voltage with an external stimulus to implement the core of a sensing device. We exploit the DC-bias voltage along with the mm-wave signal to influence the IMT/ MIT transition points. The physics of this phenomenon involve modulating the formation of conductive filaments across the thin VO_2 film. The contribution of electric fields in filament formation has been suggested by several works[24–26].

The electromagnetic power sensor is based on a two-terminal VO_2 device on which the mm-wave radiation is concentrated by an adapted antenna design (Fig. 1a), or, by directly applying a controlled power of high-frequency signal to the device under test in a dedicated setup (Fig. 1b).

By investigation of two-port S parameters and the static *I*–*V* characteristics of the VO_2 switches, we probe the transition behavior in presence of an excitation signal at different power levels.

A voltage bias enhances the VO_2 sensitivity to the incoming wave and the antennas give enhancement to the absorption. A general schematic of the setup for antenna measurements is illustrated in Fig. 1a, with high-frequency signal and the bias voltage de-coupled.

For broadband measurements, we used a CPW with the signal line interrupted by a VO_2 device. After the proof of concept by the antennas, in order to study the VO_2 response to the mm-wave power with a higher resolution, we conducted static measurements on CPW-based devices. The simplified equivalent schematic for CPW experiments is shown in Fig. 1b.

An efficient sensing configuration is proposed as depicted in Fig. 1c, by connecting the 2-terminal VO_2 device in series with a conventional MOSFET and load a capacitor in their middle point, in order to build an astable oscillator. The two alternating output

voltages of this circuit correspond the two threshold voltages of the VO_2 switch. The frequency of oscillations in the output of the circuit in Fig. 1c can be modulated by the power injected through the RF ports due to the modulation of the VO_2 threshold voltage.

According to Fig. 1d, the astability conditions are fulfilled at specific bias points where the transistor's current intersects that of the VO_2 impedance immediately after IMT threshold, as experimentally demonstrated in Supplementary materials note 1: Operational range of the spike generator. The horizontal axis is $V_{VO_2} = V_{DD} - V_{ds}$, where V_{DD} is the supply voltage at 2.5 V, and V_{ds} is the voltage between the drain and the source of the transistor in Fig. 1c.

The mm-wave signal is generated by multiplier modules connected to the vector network analyzer (VNA) and then directed to the transmission lines through GSG infinity probes. To maintain the experiments reproducible, in all the configurations a heater (as a temperature reservoir) is connected to the chuck to keep the sample at a fixed temperature. More details are found in Supplementary materials note 2: Setup Considerations.

VO_2 actuation through coupled antennas. By design and fabrication of a pair of coupled antennas, we established an experimental scheme to evaluate the VO_2 actuation through electromagnetic radiation power. At the receiver antenna, a 2-terminal VO_2 device is encapsulated inside the antenna where the incoming wave is concentrated. A cross section of the middle part inside the receiving antenna as well as a microscopic image are included in Fig. 2a, b, respectively.

The VO_2 middle volume (lateral size: $2.5 \times 10^{-5}\,\mathrm{mm}^2$) is regarded as the sensitive area of the device. The antennas of Fig. 2b are 350 µm in length, 20 µm in width, and 80 nm in thickness and have a resonance frequency around 145 GHz as shown in the return loss of Fig. 2c.

The VO_2 polycrystalline grains are revealed in the zoomed parts of Fig. 2b by scaning electron microscopy (SEM). The closer we bias the receiving antenna to the transition voltage, the more sensitive the IMT becomes to the radiation. The incident wave will add up to the threshold and actuate the metallic phase in VO_2.

A radiation between 130 GHz and 160 GHz is applied to the emitter antenna to cover the range within which the coupling between the two antennas is at a peak. The emitter antenna is identical to the receiver by the metallic pattern, while it has no VO_2 and is not biased.

The S parameters over frequencies ranging from 40 to 220 GHz are shown in Fig. 2c, d. When VO_2 is in insulating phase, the receiver antenna is terminated by the port from VNA with a standard impedance. Therefore, the impedance matching at this phase is at its highest, and so does the transmission through the antennas. As soon as VO_2 goes metallic, the antenna gets shunted by the smaller resistance of VO_2. Therefore, the value of $|S_{21}|$ gets suppressed by the change in the antenna impedance at the receiver. The receiver port matching and therefore the resonance in $|S_{11}|$ disappears as well, due to the dominant low impedance of VO_2. A theoretical simulation of the S parameters by finite element method (FEM) for different values of VO_2 conductivity is also in agreement with these results, provided in Supplementary materials note 3: Antennas Considerations.

Having the maximum $|S_{21}|$ between the antennas (−11 dB), the lower bound for insertion loss from the VNA to the VO_2 part of the antenna becomes 22 dB, excluding other potential power loss (see "Methods" section). At room temperature, even the maximum incident power to the VO_2 antenna provided by the VNA is not sufficient to cause a transition, as illustrated in Fig. 2c, d; However, the presence of a bias voltage splits the curves dramatically by VO_2 undergoing IMT due to radiation.

In the DC characteristics of the VO_2 sample of Fig. 2b, the IMT occurs near 1.713 V. The power level of 0 dBm at the VNA output (i.e. an effective power level of −22 dBm at the receiver), can split the curves for VO_2 biased at any voltage higher than 1.690 V. Closer to IMT critical voltage, for example at 1.695 V, the minimum power required to make the transition reduces to −10 dBm at VNA output (effectively −32 dBm at the receiver). Right after the event of IMT, we set the VNA power back to −30 dBm, which previously could not trigger a transition, but now the curves remain at the metallic state values. This is in complete agreement with the hysteretic characteristics of the transition. It is worth noting that by removal of the bias voltage, the backward transition (MIT) occurs immediately.

The DC characteristics of the VO_2 devices inside the antenna are depicted in Fig. 2e for different levels of mm-wave power. The distribution of these threshold voltages is found in Fig. 2f.

The equivalent RMS AC voltage amplitude corresponding to the mm-wave power that can trigger the IMT in Fig. 2c, d is smaller than the difference between the bias voltage and the threshold voltage. Reciprocally, the DC shift in the IMT threshold voltage of Fig. 2e is greater than the equivalent RMS AC voltage amplitude of the corresponding mm-wave power. A similar behavior is observed when linking the RMS AC signal to an equivalent DC voltage in a nonlinear system, for instance, when operating RF micro-electromechanical systems (MEMS) capacitive switches biased near the pull-in voltage[80].

VO_2 actuation through interrupted CPW. For a wide-band study on the VO_2-based detector, we fabricated CPWs with the signal line interrupted by a VO_2 device. Directly applying the mm-wave power through the VNA ports connected to both ends of a CPW, we try to minimize possible transmission losses, in order to extract the effect of mm-wave exposure on VO_2 DC characteristics. Using AC/DC decouplers, voltage-controlled I(V) current limited measurements were performed on the two terminals of the interrupted CPW. The CPW along with the RF probes are shown in Fig. 3a.

To characterize the transfer function of S parameters versus VO_2 state, we measured the S parameters at several temperatures from 25 °C up to 90 °C, having VO_2 through semiconducting, mixed states and metallic state. Figure 3b shows the average magnitude of S parameters for the CPW over frequencies from 60 GHz up to 110 GHz in intermediate states of VO_2 from semiconducting to metallic. Despite the relatively sharp IMT by voltage actuation, VO_2 transition has a tail in resistance versus temperature characteristics for a few Celsius degrees, as well as an observable slope. The evolution of the curves at higher temperatures is quite consistent with the gradual expansion of metallic domains in VO_2 by temperature[32]. The frequency response over this range is provided in Supplementary materials note 4: CPW S parameters.

We measured the static I–V characteristics of VO_2 inside the CPW in presence of a wide-band signal ranging from above mm-wave (60 GHz) up to 110 GHz. The curves reveal a considerable shift in the static IMT critical voltage of VO_2. At each power, 100 double-sweeps of voltage are recorded and plotted for each of Figs. 4a–c, at room temperature, 40°, and 50°, respectively. The curve-splitting gets smaller at temperatures closer to T_{IMT} as expected, besides the additional thermal fluctuations which reduce the resolution between the curves at different power levels. The extracted probability densities of the IMT threshold voltages are depicted in Figs. 4d–f for each power level. Most of the distributions cannot be fitted with normal Gaussian distribution curves and need a bimodal fitting that could relate to nonlinear phenomena specific to stochastic systems like correlated oxides.

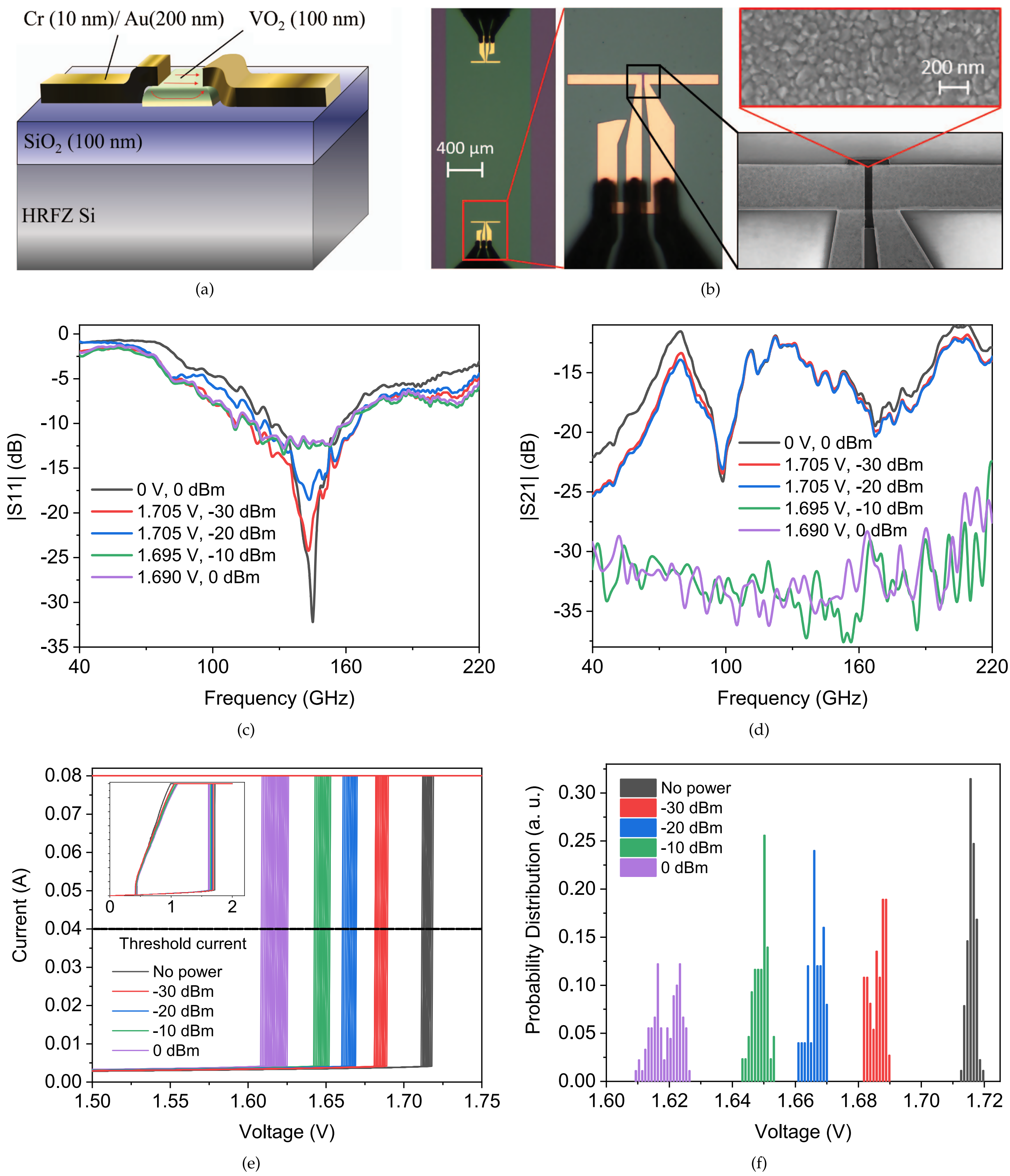

Fig. 2 Coupled dipole antennas structure and performance. a Cross section of the central part in the receiver antenna (Note: the emitting antenna has no VO_2 area), **b** microscopic image of the receiver antenna along with the zoomed SEM image, **c** $|S_{11}|$ for the emitting port for different bias voltages: impedance mismatch trend representing the transition in VO_2 shunting the receiver, **d** $|S_{21}|$ for the coupled antennas at different bias voltages: splitting curves in "on" and "off" states according to the impedance transition, **e** multicycle measurement of *I*–*V* characteristics for VO_2 in the receiving antenna, showing the shift in the IMT threshold voltage according to the external power. Inset: an overview of the whole characteristics, **f** probability density of IMT threshold voltages at each power.

Astable circuit. The 2-terminal VO_2 devices function as active elements in the astable multivibrator circuit of Fig. 1c. The output signal of the oscillator was recorded for several thousands of cycles at each power level. We notice that the average of the IMT threshold voltage (V_{IMT}) sensitivity to the incident power is much higher than that of the average MIT threshold voltage (V_{MIT}). Thus, we obtain a modulation of the hysteresis window width as a function of applied external RF power.

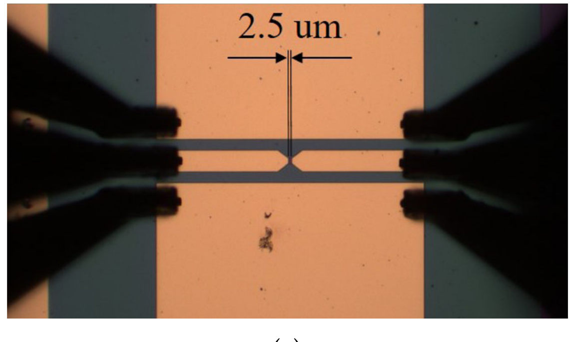

(a)

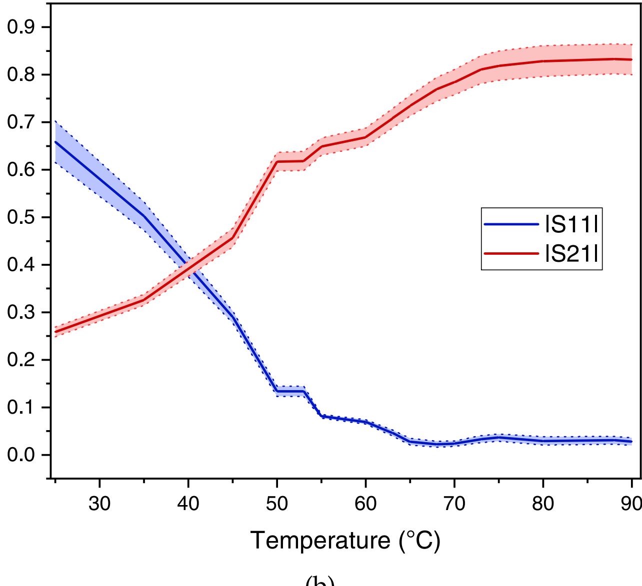

(b)

Fig. 3 Interrupted CPW by VO_2 structure and S parameters behavior. **a** Under the microscope, **b** S parameters magnitude between the two ports across the CPW vs. temperature. The standard deviation is represented as the shades around the curves.

Any change in the IMT threshold voltage modulates the intersection of the VO_2 device I–V characteristics with that of the transistor in a series configuration (Fig. 1d). As long as the excursion of the operating point does not reach the triode region of the MOSFET, any change in hysteresis window width will translate into a proportional change in operating frequency, as shown in the fast Fourier transform (FFT) spectra of Fig. 5a. The FFT is performed using a rectangular window over an interval of 3 s.

The histograms at each power level (Fig. 5c–h) show bimodal distributions which can be related to the threshold voltage distributions of Fig. 4d–f through the nonlinear oscillator transfer function. Every waveform is recorded for about 3 s and every cycle is converted to an equivalent frequency to be compared statistically.

Based on Allan deviation calculations, we were able to identify four main noise behaviors. One related to thermal noise, leads to a Normal statistic and dominates for averaging times below 200 ms. The lowest noise level around 200 ms is usually related to 1/f (Flicker) noise. The next rise in the distribution noise can be related to the nucleation Poissonian processes and dominates for longer time constants. Final bumps are mostly due to parasitic signals, inter-modulation, low-frequency interference, instabilities of supply voltage, etc. It then limits the potential averaging of successive frequency measurements to reduce their standard deviation. Both mechanisms combine to induce threshold fluctuations, act as precursors of a bifurcation, and appear to form the basis of the stochastic oscillating behavior.

Detection capability. The shift in the static IMT critical voltage in presence of a high-frequency signal, with respect to the baseline static curve (the one with no additional high-frequency power), is a criterion for the "response" of the VO_2-based devices. Using a proper read-out circuit, one can exploit the sensing capability of such a response in mm-wave and THz applications. Responsivity, or R_V, defined as the ratio of the shift in the required voltage for IMT to the radiation power from the emitting port, is plotted in Fig. 6a versus the corresponding power: $R_V = \frac{\Delta V}{P}$, where ΔV is the shift in the static threshold voltage regarding the applied power (P). The responsivity in Fig. 6a is based on the nominal power from the source, while if we consider only the received power by the VO_2 sensing area, the responsivity gets at least one order of magnitude higher.

We apply a similar concept for responsivity in the frequency shift of oscillations, defined by the deviation in the central frequency of oscillations divided by the corresponding power: $R_f = \frac{\Delta f}{P}$, where Δf is the shift in the frequency of oscillations with respect to the reference frequency. The reference frequency is attributed to the free running oscillation under no applied power (Fig. 5a).

The noise equivalent power (NEP) of a detector is theoretically defined as the ratio between the noise power spectral density and the responsivity. One source of the noise in this detector is the VO_2 resistance and therefore responsible for Johnson-Nyquist noise, which depends on temperature and resistance by $\sqrt{4k_B TR\Delta f}$, where R is the resistance of the active detecting area and Δf is the measurement single-sided bandwidth. Based on the insulating phase, where the resistance of the device is maximum 1.4 kΩ, the upper bound for the Johnson-Nyquist noise is evaluated 4.8 nV.Hz$^{-1/2}$. This is a simplified estimation of the noise spectral density. Another source is the shot noise of the bias current. The root mean square (RMS) current fluctuations as a Poisson process has a magnitude of $\sqrt{2qI_{dc}\Delta f}$, where q is the charge of an electron and I_{dc} is the bias current. In order to experimentally evaluate the noise in static measurements, we apply a constant voltage close to V_{IMT} and record the fluctuations in the current over 200 s, and calculate the NEP down to 4 mHz through the FFT of the signal fluctuations (Fig. 6b). In an alternative measurement, we fixed the current and measured the voltage fluctuations. The results for both show relatively the same levels of noise, which we attribute more to external sources and the setup.

The procedure of extracting the NEP: We normalize the FFT of the current-fluctuations-voltage-product by the bandwidth and extract the integrated output noise power ($P_{N,out}$) through the analysis described in the Supplementary materials note 5: NEP evaluation. The noise spectral density (NSD) voltage would be equal to $v_n = \sqrt{P_{N,out}.R_L}$.

Where R_L is the measurement tool impedance, typically 50 Ω. The equivalent input noise power ($P_{N,in}$) is then evaluated by normalizing v_n by the voltage responsivity: $P_{N,in} = v_n/R_V$. The responsivity value used here is the one at the smallest power detected. Finally, to achieve the NEP we divide this power by the $\sqrt{BW}$. For the case of static detection, a value of 1 Hz is set as the BW.

The maximum NEP among all the cases happens when the temperature goes high enough so that the degradation in responsivity dominates the decline in resistance, which explains

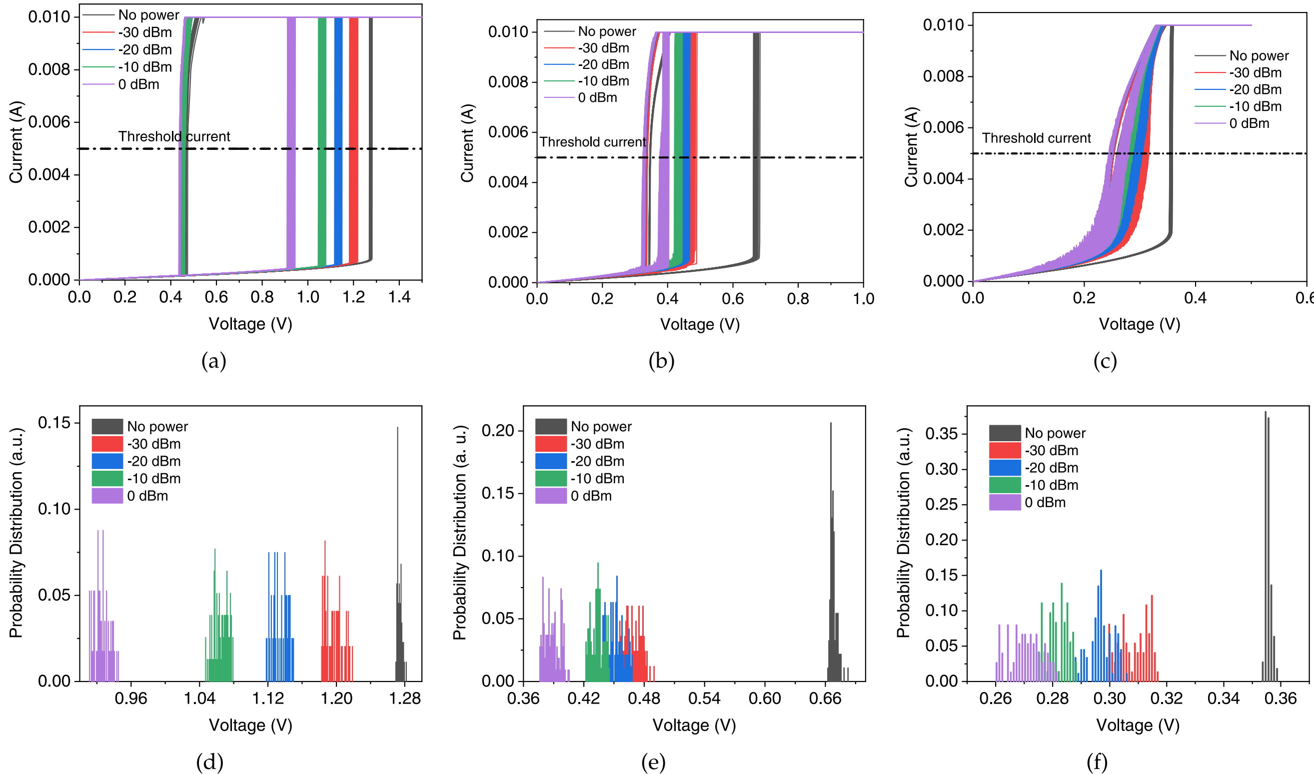

Fig. 4 IMT threshold voltage distribution with respect to the mm-wave power. **a–c** Static *I–V* characteristics of VO_2 with respect to different levels of external power, at **a** room temperature, **b** 40 °C, and **c** 50 °C. Probability distribution of IMT threshold voltage, at **d** room temperature, **e** 40 °C, and **f** 50 °C. Elevated temperatures make major shifts in the threshold voltage, while the effect of the external power is maintained in all cases. The temperature role is mainly on the resolution between the curves at different power levels.

the worst NEP in CPW devices at 50° C. At room temperature, we consider the worst NEP at low frequencies, which includes collectively the effect of material drifts, thermal fluctuations, flicker noise, and the external noise coming from the ambient setup. The upper bound of the NEP in this case is near 5 nW.Hz$^{-0.5}$ for frequencies higher than 1 Hz.

We also consider the intrinsic noise of the stochastic behavior in phase transition. The fitted standard deviation (σ) of (V_{IMT}) in CPW devices at room temperature, which is 2.77 mV when no power applied, determines the LoD. The LoD can be estimated by $3\sigma/R_{\mathrm{V}}$ at lowest actuation level, which gives the value of 68.7 nW. However, the standard deviation for the frequency of oscillations according to Allan method[81] goes down to 1.3 Hz for averaging times around 200 ms when no power or very low power is applied (Fig. 6c). In this case the equivalent LoD will be 58 nW. The detailed LoD values at different power levels can be found in Supplementary materials note 6: Detailed LoD values.

Using the electrical responsivity, the minimum detectable signal (at SNR = 1) or the "electrical NEP", represents the intrinsic performance limitations of the device. While the optical NEP is equal to the ratio of the electrical NEP and the optical coupling efficiency of the detector system[82]. As we consider the emitted power by the VNA and not the absorbed one at the sensor spot, the evaluated responsivity and NEP are normalized by the coupling efficiency. Hence, we report an upper bound for the external NEP in this work.

Response time. In the experimental investigations based on application of electrical pulses, the IMT response time goes down to sub-nanosecond, and the MIT down to about one microsecond[83]. For direct measurements, every single acquisition will depend on the ramp generator speed as well as the probing instrument sampling rate. Every forward sweep in our case takes at least 200 ns to log a single phase transition (more explanations in Supplementary materials note 2: setup considerations).

For multicycle acquisition the reset time imposes a delay time of at least 1 µs. In the astable circuit, besides the material response time, the RC circuit time constant is also determining the timescales. It is 210 µ*s* and 9 µs for "off" and "on" states, based on the 150 nF capacitor along with the effective resistance (VO_2 impedance in parallel with the transistor output resistance), while VO_2 impedances of 1.4 kΩ and 60 Ω for "off" and "on" states are dominant, respectively. It is worth noting that the experimental integration time in this case determines the duration of each acquisition. If we aim for the minimum NEP, we have to use more cycles of the same measurement, at least about 100 ms according to Allan method for this experiment, as in Fig. 6c.

We have investigated the timescales of partial switching through two-terminal VO_2 devices inside a CPW by applying a single-tone RF signal on one side and monitoring the same component on the other side by means of a spectrum analyzer. When no bias voltage is applied to the material, the output component is at the level of the noise floor by the spectrum analyzer. While in presence of a bias voltage right below the MIT threshold voltage, the component shows up as a demonstration of the material switching. The amplitude modulated THz measurements suggest a cut-off frequency (−3 dB) of 12 GHz for VO_2 partial switching in the hysteresis region of the material[84].

Discussion

The demonstration room temperature actuation of VO_2 by mm-wave and THz applied power proves the opportunity of designing and manufacturing efficient sensor devices based on the phase change phenomena. We first improved the sensitivity of VO_2 to

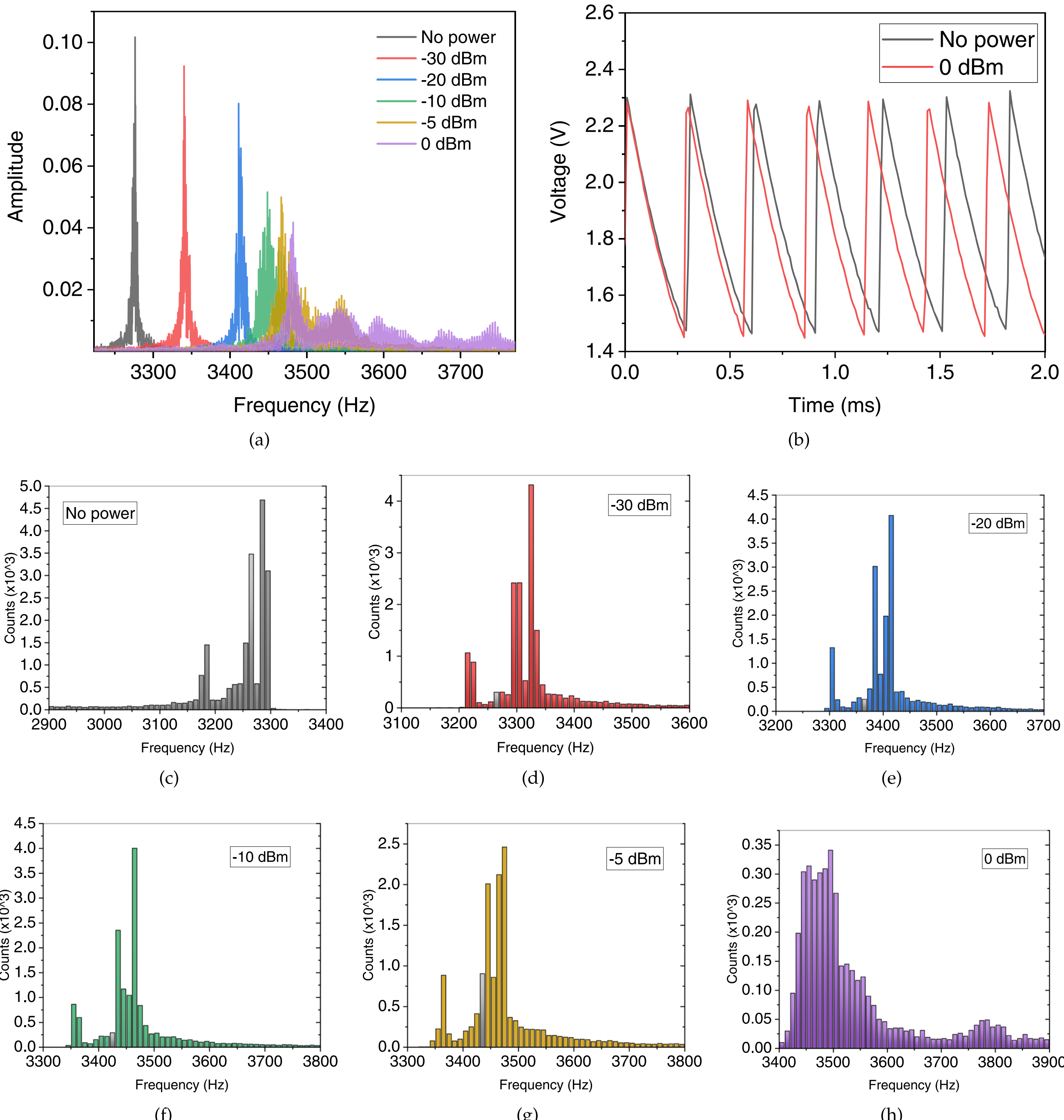

Fig. 5 Distribution of the frequency of oscillations based on the mm-wave power. a FFT of output waveforms with respect to the applied power, **b** time domain waveforms of the astable output signal for "no power" and "0 dBm" exposure, **c**–**h** the distribution of the frequency of oscillations based on the emitted power from the first port: every waveform is recorded for about 3 s and every cycle is converted to an equivalent frequency to be compared statistically.

low-power radiation by means of a DC-bias-assisted setting inside an antenna and investigated its properties in a CPW configuration.

We demonstrated the density-driven IMT by radiation in VO_2 through splitting the S parameters in a two-coupled-antenna setup, where VO_2 is embedded in one of them. Furthermore, the effect of external radiation on the static I-V characteristics of VO_2 is shown as a shift in the threshold voltage required to induce IMT. This effect can form the principle of detection in mm-wave and THz detectors. We reported the extent of this shift normalized by the radiation power as the nominal responsivity of the device in Fig. 6a. This is while the actual responsivity as a function of absorbed power is at least 37 s higher than the values reported in this figure for the case of the antennas, and more than three times higher in the case of CPWs. With this definition, the equivalent noise power will also get lower proportionally.

The non-deterministic behavior of threshold voltage in VO_2 has roots in the nucleation processes responsible for the filament formation in a polycrystalline VO2 film. In each cycle of switching, the formation of paths can vary according to the local temperature and free electron distribution densities between the grains[85]. The switching voltage distribution can also be influenced

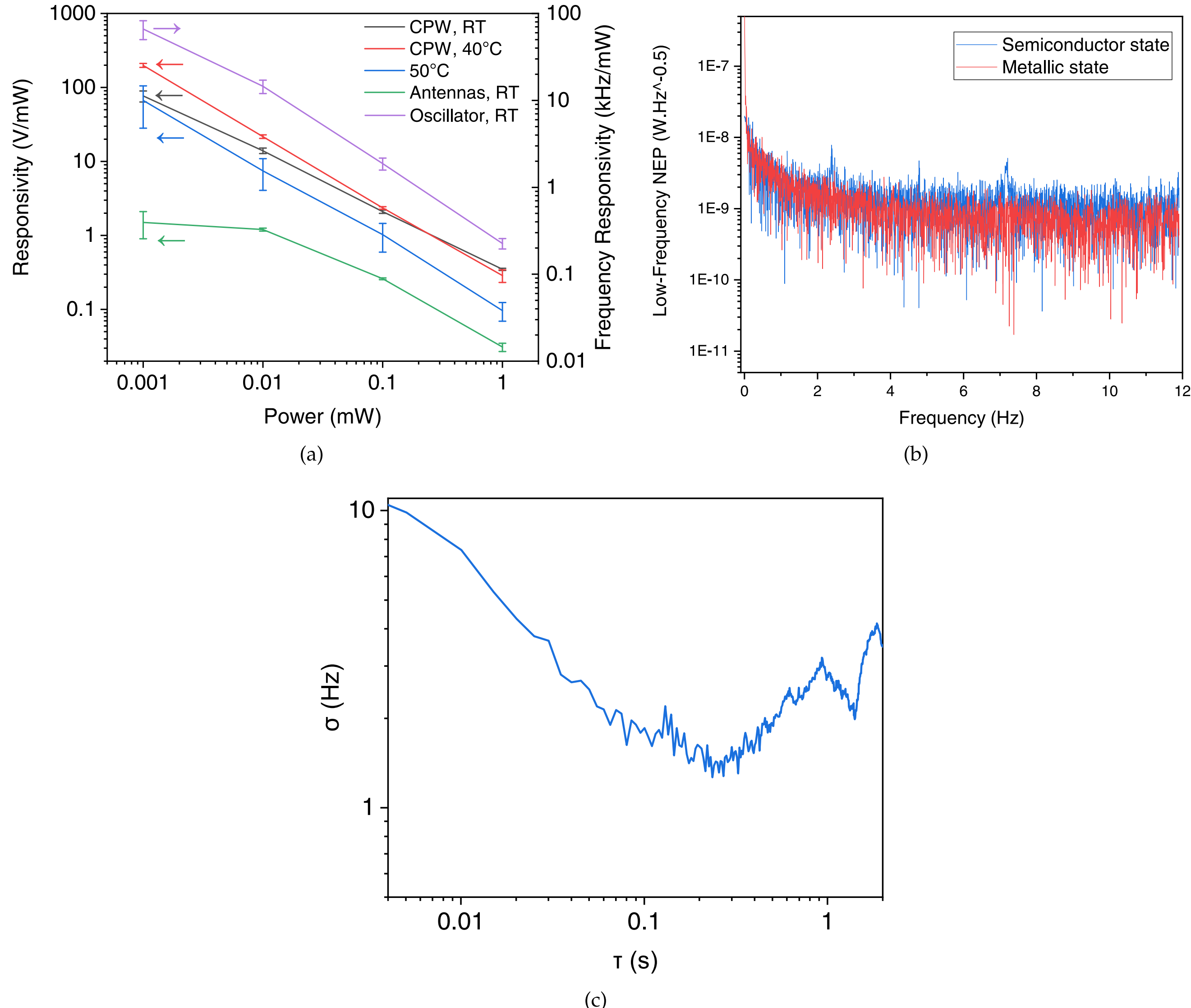

Fig. 6 Performance figures of merit for the proposed VO_2-based sensor. a DC and frequency responsivity due to the shift in the IMT threshold voltage for the mentioned configurations based on the emitted power from the first port. The error bars represent the standard deviation according to repetitive runs of measurements (at least 100 cycles for DC responsivity measurements and thousands of cycles for the oscillator response). **b** Noise equivalent power of the CPW devices at very low frequencies, at the minimum measured signal (1 μW), **c** Allan deviation calculation on the frequency vs time measurements of the oscillator over a long duration of time, no external power applied.

by non-stoichiometric parts of the film, such as variations in oxygen vacancies in different grains as in ref. [86]. A more general description for the non-stoichiometric effects are crystal defects. Grain boundaries also play a critical role in conduction and switching behavior[87]. Thanks to Allan deviation calculations, the uncertainty of power detection is reduced by almost one order of magnitude as inferred from Fig. 6c.

Concerning the nonlinear responsivity in Fig. 6a, the extent of the shift at the lowest incident power compared to the shift due to higher levels of power, confirms that the sensor shows a higher responsivity to smaller triggers. According to NEP = NSD/R_V, the higher responsivity at smaller excitations which are prone to a lower signal to noise ratio, allows more efficiency in low-signal detection. The equivalent RMS AC voltage is smaller than the actual DC shift that it causes. Such behavior is usually found in avalanche phenomena, and here it can relate to the lattice instabilities driving the phase transition at a proper bias point. Hence, by device scaling and bias point engineering, the figures of merit have room to be enhanced.

The reversible electric-field-induced hysteresis loop has shown robustness over millions of non-stop switching cycles in our oscillator measurements. The same devices have been measured over days, showing the same V_{IMT} and V_{MIT} threshold voltages. We inspected the degradation and aging of the VO_2 film regarding the switching and the ratio of resistance between the two states in Supplementary materials note 7: VO2 film investigation.

The response time of detectors based on a thermal process is usually longer than that of an electrical mechanism. The response time of our proposed sensor system is about 308 μs (mostly dictated by the readout instruments, not a VO_2 intrinsic characteristic), while it is about 83 ms for one of the latest state-of-the-art bolometers based on VO_2[68].

Regarding sensor applications, the above-described method and devices appear to be applicable over a relatively wide range in temperature from cooled conditions (the IMT voltage is always assisted by a calibrated DC voltage) up to around 40° C. The experimental figures of merit of the power sensor proposed here

Table 1 Comparison of the detector performances in different technologies.

Detector type	R_V	NEP [nW Hz$^{-0.5}$]	Frequency (THz)	Response time	Ref.
Graphene-based	20–600 V W^{-1}	0.08–1	0.01–0.8/ 1.8–4.25	1 ns to 9 μs	48,49,51–55
Si FET	10–5000 V W^{-1}	0.01–199	0.1–4.52	10 μs to 100 ms	39–46
Tunneling rectifier	4 kV W^{-1}	2×10^{-4}	0.13	NA	56
Schottky diode	100–1000 V W^{-1}	4×10^{-3}–1	0.1–1	0.1 ns	57,58
Microbolometer	500–760 V W^{-1}	0.1–0.2	1	140 μs	61,62
[a]VO_2-based oscillator	21.28 GHz/W	NA	Optical	10 μs	74
VO_2-based bolometer	36.9–124 V W^{-1}	NA	0.075–0.11	83 ms	64,68
This work	DC: 76 kV/W, AC: 66.3 MHz/W	5	0.01–0.22	308 μs	

[a]The VO_2-based oscillator of ref. [74] works in the visible range, and the central frequency of oscillations is within the range of MHz, so between 2 and 3 orders of magnitude higher than the carrier frequency of our setup. In this case, the frequency resolution or the normalized responsivity to the carrier frequency should be considered.

are compared to other works that report power sensing based on graphene, Silicon FETs, and some other VO_2-based devices as summarized in Table 1.

The idea of utilizing nonlinearity for detection is also explored in tunneling devices where steep I–V curves result in strong rectification of incident electromagnetic fields[56,88,89].

Our results suggest that for the design and performance optimization of a spiking VO_2 sensor, it is important to: (i) design low-voltage actuation of structures (similarly with low-voltage-actuated MEMS with soft springs), therefore further miniaturization of device length and field concentrators are expected to help further enhancement of the sensing characteristics, (ii) improve the high-frequency power coupling into the 2-terminal VO_2 device by better antennas and CPW design and reduce the parasitic effects, (iii) consider operating the device near the switching point and combine with the use of a local heater.

In general VO_2 is a strong candidate for any type of applications requiring tunable materials. They provide an unprecedented ability for electromagnetic wave manipulation, particularly at THz frequencies. As for the particular detector reported in this work, a few applications are: (i) absolute THz power meters - for which our solution can provide a simpler and more cost-effective solution, (ii) sensing THz waves in a chip-scale technology that are currently emerging and for which the exact specifications are more difficult to be articulated, but can take benefit from or on-chip scalable VO_2 devices that can support building arrays of detectors.

Methods

VO_2 deposition. During the development of pulsed laser deposition (PLD) VO_2 films at EPFL center of micro/nano-engineering clean room, we have selected the set of parameters (oxygen flow, pressure and temperature of annealing) that were producing the highest R_{On}/R_{Off} and most reproducible results. The thin film deposition is done on a 525 μm-thick high resistivity float zone (HRFZ) Si wafer (>10,000 Ω cm). The substrate was then passivated by growth of 2 μm SiO_2 thermal wet oxide. The 100-nm-thick polycrystalline VO_2 film was synthesized on this substrate through a PLD system using a V_2O_5 target, in high-vaccum conditions, in a chamber with pressure of 0.01 mbar and Oxygen flow of 1 sccm. The laser energy was 400 mJ with a pulse frequency of 20 Hz. The substrate temperature was kept at 400 °C during the deposition, and the process was followed by post annealing at 475 °C. We have also controlled the purity of the VO_2 films and systematically checked no metal contamination in our samples. In this process, one achieves polycrystalline VO_2. However, there are other processes leading to mono-oriented VO_2 film deposition. For instance, using monocrystalline Al_2O_3, which has a relatively low lattice parameter mismatch (4.5%) compared to VO_2 monoclinic phase. The polycrystalline film on top of Si/SiO_2 shows an overall lower On/Off ratio of conductivity with respect to that of a monocrystalline.[16,17].

Device fabrication. The VO_2 film was patterned on a 100-nm-thick SiO_2 layer, using photolithography on negative tone AZ nLof 2020 resist followed by wet etching in diluted Cr etch solution. For the second layer, 15 nm Cr was sputtered on the patterned substrate as an interface layer and the process was followed by the sputtering of 150 nm Au. The connections and the 2-terminal devices were completed by dry etching of the sputtered metal using a broad beam of Argon ions in an ion-beam-etcher. A more detailed process flow is presented in the Supplementary materials note 8: Fabrication Process.

Electrical measurements. High and low-frequency measurements were all performed on a Cascade Summit probe station. Mm-wave measurement incorporated broadband VNA system with MPI GSG 220-GHz infinity probes, each of them connected to a port from ANRITSU Vector Star VNA through frequency multiplier modules based on nonlinear transmission line (NLTL).

DC measurements were planned on a multicycle mode using Keithley semiconductor parameter analyzer. Each series of the DC measurements were performed at least a hundred cycles in a row to avoid transient results for the static characteristics of VO_2.

Antennas. According to Fig. 2d, the $|S_{21}|$ between the two ports is about −11 dB at its highest. We consider it when estimating the absorbed power by the VO_2-based antenna. Power loss also takes place through the cables, the transition from the infinity probes to the transmission line, the transition from the line to the dipole antenna, the return loss, and the reciprocal form of the mentioned transitions on the way to the receiving port.

According to the specifications in the frequency we use, the upper bound for the $|S_{21}|$ of the cables (Rosenberger RU5-08S1-08K1-00915 and TOTOKU TCF119XY100S2p) is collectively about −4 dB and the upper bound for that of an infinity probe is about −0.7 dB. We only estimated the lower band of losses on the results section, assuming that the mentioned ones here are addressed through the calibration.

Data availability

All the relevant data supporting the results of this study are available from the corresponding authors upon request.

Received: 6 June 2022; Accepted: 21 March 2023;
Published online: 22 May 2023

References

1. Morin, F. J. Oxides which show a metal-to-insulator transition at the neel temperature. *Phys. Rev. Lett.* **3**, 34–36 (1959).
2. Berglund, C. & Guggenheim, H. Electronic properties of VO2 near the semiconductor-metal transition. *Phys. Rev.* **185**, 1022 (1969).
3. Pellegrino, L. et al. Multistate memory devices based on free-standing VO2/tio2 microstructures driven by joule self-heating. *Adv. Mater.* **24**, 2929–2934 (2012).
4. Cabrera, R., Merced, E. & Sepúlveda, N. A micro-electro-mechanical memory based on the structural phase transition of VO2. *Phys. Status Solidi (a)* **210**, 1704–1711 (2013).
5. Mazza, G., Amaricci, A., Capone, M. & Fabrizio, M. Field-driven mott gap collapse and resistive switch in correlated insulators. *Phys. Rev. Lett.* **117**, 176401 (2016).
6. Kalcheim, Y. et al. Robust coupling between structural and electronic transitions in a mott material. *Phys. Rev. Lett.* **122**, 057601 (2019).
7. Miller, K. J., Hallman, K. A., Haglund, R. F. & Weiss, S. M. Silicon waveguide optical switch with embedded phase change material. *Opt. Express* **25**, 26527–26536 (2017).

8. Fan, L. et al. Infrared response and optoelectronic memory device fabrication based on epitaxial VO2 film. *ACS Appl. Mater. Interfaces* **8**, 32971–32977 (2016).
9. Koledov, V. et al. Interaction of electromagnetic waves with VO2 nanoparticles and films in optical and millimetre wave ranges: Prospective for nano-photonics, nano-antennas, and sensors. *J. Phys. Confer. Ser.* **1092**, 012108 (2018).
10. Kim, B.-J. et al. Temperature dependence of the first-order metal-insulator transition in vo 2 and programmable critical temperature sensor. *Appl. Phys. Lett.* **90**, 023515 (2007).
11. Benkahoul, M. et al. Thermochromic VO2 film deposited on al with tunable thermal emissivity for space applications. *Sol. Energy Mater. Sol. Cells* **95**, 3504–3508 (2011).
12. Lei, L. et al. Tunable and scalable broadband metamaterial absorber involving VO2-based phase transition. *Photon. Res.* **7**, 734–741 (2019).
13. Brockman, J. S. et al. Subnanosecond incubation times for electric-field-induced metallization of a correlated electron oxide. *Nat. Nanotechnol.* **9**, 453–458 (2014).
14. Lappalainen, J., Mizsei, J. & Huotari, M. Neuromorphic thermal-electric circuits based on phase-change VO2 thin-film memristor elements. *J. Appl. Phys.* **125**, 044501 (2019).
15. Corti, E. et al. Scaled resistively-coupled VO2 oscillators for neuromorphic computing. *Solid State Electron.* **168**, 107729 (2020).
16. Crunteanu, A. et al. Voltage- and current-activated metal-insulator transition in VO2-based electrical switches: a lifetime operation analysis. *Sci. Technol. Adv. Mater.* **11**, 065002 (2010).
17. Dumas-Bouchiat, F., Champeaux, C., Catherinot, A., Crunteanu, A. & Blondy, P. Rf-microwave switches based on reversible semiconductor-metal transition of vo 2 thin films synthesized by pulsed-laser deposition. *Appl. Phys. Lett.* **91**, 223505 (2007).
18. Ghann, W. & Uddin, J. Terahertz (THz) spectroscopy: A cutting edge technology. In *Terahertz Spectroscopy-A Cutting Edge Technology* (InTech, 2017).
19. Kulesa, C. Terahertz spectroscopy for astronomy: From comets to cosmology. *IEEE Transactions on Terahertz Science and Technology* **1**, 232–240 (2011).
20. Choudhury, B., Menon, A. & Jha, R. M. *Active Terahertz Metamaterial for Biomedical Applications*, 1–41 (Springer Singapore, Singapore, 2016).
21. Mittleman, D. M. Twenty years of terahertz imaging. *Opt. Express* **26**, 9417–9431 (2018).
22. Corsi, C. & Sizov, F. *THz and Security Applications: Detectors, Sources and Associated Electronics for THz Applications* (Springer, 2014).
23. Koenig, S. et al. Wireless sub-THz communication system with high data rate. *Nat. Photonics* **7**, 977–981 (2013).
24. Duchene, J., Terraillon, M., Pailly, P. & Adam, G. Filamentary conduction in VO2 coplanar thin-film devices. *Appl. Phys. Lett.* **19**, 115–117 (1971).
25. Lee, J., Ortolani, M., Schade, U., Chang, Y. & Noh, T. Microspectroscopic detection of local conducting areas generated by electric-pulse-induced phase transition in vo 2 films. *Appl. Phys. Lett.* **91**, 133509 (2007).
26. Lee, J. et al. Electric-pulse-induced local conducting area and joule heating effect in VO2/al2o3 films. *Infrared Phys. Technol.* **51**, 443–445 (2008).
27. Okimura, K., Ezreena, N., Sasakawa, Y. & Sakai, J. Electric-field-induced multistep resistance switching in planar VO2/c-al2o3structure. *Jpn. J. Appl. Phys.* **48**, 065003 (2009).
28. Pevtsov, A. B. et al. Evidence of field-induced nucleation switching in opal: VO_2 composites and vo_2 films. *Phys. Rev. B* **85**, 024110 (2012).
29. Gopalakrishnan, G., Ruzmetov, D. & Ramanathan, S. On the triggering mechanism for the metal–insulator transition in thin film vo 2 devices: electric field versus thermal effects. *J. Mater. Sci.* **44**, 5345–5353 (2009).
30. Diener, P. et al. How a dc electric field drives mott insulators out of equilibrium. *Phys. Rev. Lett.* **121**, 016601 (2018).
31. Stoliar, P. et al. Nonthermal and purely electronic resistive switching in a mott memory. *Phys. Rev. B* **90**, 045146 (2014).
32. Yang, Z., Ko, C. & Ramanathan, S. Oxide electronics utilizing ultrafast metal-insulator transitions. *Annu. Rev. Mater. Res.* **41**, 337–367 (2011).
33. Kalcheim, Y. et al. Non-thermal resistive switching in mott insulator nanowires. *Nat. Commun.* **11**, 1–9 (2020).
34. Bohaichuk, S. M. et al. Localized triggering of the insulator-metal transition in VO2 using a single carbon nanotube. *ACS Nano* **13**, 11070–11077 (2019).
35. Mayer, B. et al. Tunneling breakdown of a strongly correlated insulating state in v o 2 induced by intense multiterahertz excitation. *Phys. Rev. B* **91**, 235113 (2015).
36. Cocker, T. et al. Time-resolved THz spectroscopy of the ultrafast photoinduced insulator-metal phase transition of VO2. In *Proc International Conference on Ultrafast Structural Dynamics*, IT4D-3 (Optical Society of America, 2012).
37. Tao, Z. et al. The nature of photoinduced phase transition and metastable states in vanadium dioxide. *Sci. Rep.* **6**, 1–10 (2016).
38. Liu, M. et al. Terahertz-field-induced insulator-to-metal transition in vanadium dioxide metamaterial. *Nature* **487**, 345–348 (2012).
39. Khan, M. I. W. et al. Nonlinear analysis of nonresonant THz response of mosfet and implementation of a high-responsivity cross-coupled THz detector. *IEEE Trans. Terahertz Sci. Technol.* **8**, 108–120 (2018).
40. Deng, X., Simanullang, M. & Kawano, Y. Ge-core/a-si-shell nanowire-based field-effect transistor for sensitive terahertz detection. In *Photonics*, vol. 5, 13 (Multidisciplinary Digital Publishing Institute, 2018).
41. Ponomarev, D. et al. Sub-terahertz fet detector with self-assembled sn-nanothreads. *J. Phys. D Appl. Phys.* **53**, 075102 (2019).
42. Kopyt, P., Salski, B., Pacewicz, A., Zagrajek, P. & Marczewski, J. Measurements of the responsivity of fet-based detectors of sub-THz radiation. *Opto Electron. Rev.* **27**, 123–129 (2019).
43. Ikamas, K., Nevinskas, I., Krotkus, A. & Lisauskas, A. Silicon field effect transistor as the nonlinear detector for terahertz autocorellators. *Sensors* **18**, 3735 (2018).
44. Qayyum, S. & Negra, R. 0.8 mw, 0.1–110 GHz rf power detector with 6 GHz video bandwidth for multigigabit software defined radios. In *Proc 2017 IEEE MTT-S International Microwave Symposium (IMS)*, 1722–1725 (IEEE, 2017).
45. Javadi, E. et al. Sensitivity of field-effect transistor-based terahertz detectors. *Sensors* **21**, 2909 (2021).
46. Andersson, M. A. & Stake, J. An accurate empirical model based on Volterra series for fet power detectors. *IEEE Trans. Microw. Theory Tech.* **64**, 1431–1441 (2016).
47. Nahar, S. et al. Wide modulation bandwidth terahertz detection in 130 nm cmos technology. *Eur. Phys. J. Appl. Phys.* **76**, 20101 (2016).
48. Viti, L., Purdie, D. G., Lombardo, A., Ferrari, A. C. & Vitiello, M. S. Hbn-encapsulated, graphene-based, room-temperature terahertz receivers, with high speed and low noise. *Nano Lett.* **20**, 3169–3177 (2020).
49. El Fatimy, A. et al. Ultra-broadband photodetectors based on epitaxial graphene quantum dots. *Nanophotonics* **7**, 735–740 (2018).
50. Ma, W. et al. Ultrabroadband tellurium photoelectric detector from visible to millimeter wave. *Advanced Science* **9**, 2103873 (2022).
51. Rama Murali, G. K., Deshmukh, P., Prabhu, S. S. & Basu, P. K. Antenna coupled graphene-fet as ultra-sensitive room temperature broadband THz detector. *AIP Adv.* **8**, 125122 (2018).
52. Bandurin, D. et al. Dual origin of room temperature sub-terahertz photoresponse in graphene field effect transistors. *Appl. Phys. Lett.* **112**, 141101 (2018).
53. Generalov, A. A., Andersson, M. A., Yang, X., Vorobiev, A. & Stake, J. A 400-GHz graphene fet detector. *IEEE Trans. Terahertz Sci. Technol.* **7**, 614–616 (2017).
54. Tong, J. et al. Asymmetric 2-terminal graphene detector for broadband radiofrequency heterodyne-and self-mixing. *Nano Lett.* **18**, 3516–3522 (2018).
55. Castilla, S. et al. Fast and sensitive terahertz detection using an antenna-integrated graphene pn junction. *Nano Lett.* **19**, 2765–2773 (2019).
56. Gayduchenko, I. et al. Tunnel field-effect transistors for sensitive terahertz detection. *Nat. Commun.* **12**, 1–8 (2021).
57. Daghestani, N. et al. Room temperature ultrafast ingaas schottky diode based detectors for terahertz spectroscopy. *Infrared Phys. Technol.* **99**, 240–247 (2019).
58. Harter, T. et al. Wireless thz link with optoelectronic transmitter and receiver. *Optica* **6**, 1063–1070 (2019).
59. Yardimci, N. T. & Jarrahi, M. High sensitivity terahertz detection through large-area plasmonic nano-antenna arrays. *Sci. Rep.* **7**, 1–8 (2017).
60. Siday, T. et al. Terahertz detection with perfectly-absorbing photoconductive metasurface. *Nano Lett.* **19**, 2888–2896 (2019).
61. Aji, A. P., Satoh, H., Apriono, C., Rahardjo, E. T. & Inokawa, H. Responsivity and nep improvement of terahertz microbolometer by high-impedance antenna. *Sensors* **22**, 5107 (2022).
62. Banerjee, A. et al. Performance improvement of on-chip integrable terahertz microbolometer arrays using nanoscale meander titanium thermistor. *J. Appl. Phys.* **125**, 214502 (2019).
63. Marczewski, J., Knap, W., Tomaszewski, D., Zaborowski, M. & Zagrajek, P. Silicon junctionless field effect transistors as room temperature terahertz detectors. *J. Appl. Phys.* **118**, 104502 (2015).
64. Tachiki, T. & Uchida, T. et al. Fabrication and evaluation of thin-film spiral-antenna-coupled vox microbolometer by metal–organic decomposition. *Jpn. J. Appl. Phys.* **52**, 046601 (2013).
65. Chen, S., Lust, M. & Ghalichechian, N. Multiphysics simulation of hypersensitive microbolometer sensor using vanadium dioxide and air suspension for millimeter wave imaging. *Microsyst. Technol.* **27**, 2815–2822 (2021).
66. De Almeida, L. et al. Modeling and performance of vanadium–oxide transition edge microbolometers. *Appl. Phys. Lett.* **85**, 3605–3607 (2004).
67. Kil, T.-H. et al. Selective growth and texturing of VO2 (b) thin films for high-temperature microbolometers. *J. Eur. Ceram. Soc.* **40**, 5582–5588 (2020).
68. Zhang, Y. et al. Highly sensitive and ultra-broadband VO2 (b) photodetector dominated by bolometric effect. *Nano Lett.* **22**, 485–493 (2021).

69. Pan, M. et al. Properties of VO2 thin film prepared with precursor vo (acac) 2. *J. Cryst. Growth* **265**, 121–126 (2004).
70. Neto, G. et al. Figures of merit and optimization of a VO2 microbolometer with strong electrothermal feedback. *Opt. Eng.* **47**, 073603 (2008).
71. Chen, X. & Lv, Q. Resistance hysteresis loop characteristic analysis of VO2 thin film for high sensitive microbolometer. *Optik* **126**, 2718–2722 (2015).
72. Dem'yanenko, M., Marchishin, I. & Startsev, V. Absorption of terahertz radiation by a thin metal absorber in conventional and inverted bolometers. *OSA Contin.* **2**, 2085–2097 (2019).
73. Aliev, V. S. & Bortnikov, S. G. Bolometer at semiconductor-metal phase transition in vo 2 thin films. In *Proc 2011 International Conference and Seminar on Micro/Nanotechnologies and Electron Devices Proceedings*, 129-131 (IEEE, 2011).
74. Kim, B.-J., Seo, G., Choi, J., Kim, H.-T. & Lee, Y. W. Laser-assisted control of electrical oscillation in VO2 thin films grown by pulsed laser deposition. *Jpn. J. Appl. Phys.* **51**, 107302 (2012).
75. Cosci, A. et al. Thz pyro-optical detector based on linbo3 whispering gallery mode microdisc resonator. *Sensors* **17**, 258 (2017).
76. Rosca, T., Qaderi, F. & Ionescu, A. M. High tuning range spiking 1r-1t vo 2 voltage-controlled oscillator for integrated rf and optical sensing. In *Proc ESSCIRC 2021-IEEE 47th European Solid State Circuits Conference (ESSCIRC)*, 183-186 (IEEE, 2021).
77. Chen, C. & Zhou, Z. Optical phonons assisted infrared absorption in VO2 based bolometer. *Appl. Phys. Lett.* **91**, 011107 (2007).
78. Li, G. et al. Photo-induced non-volatile vo2 phase transition for neuromorphic ultraviolet sensors. *Nat. Commun.* **13**, 1–9 (2022).
79. Tadjer, M. J. et al. Temperature and electric field induced metal-insulator transition in atomic layer deposited VO2 thin films. *Solid State Electron.* **136**, 30–35 (2017).
80. Vitale, W. A., Fernández-Bolaños, M., Bazigos, A., Dehollain, C. & Ionescu, A. M. Rf mems power sensors for ultra-low power wake-up circuit applications. In *2013 Proceedings of the European Solid-State Device Research Conference (ESSDERC)*, Bucharest, Romania, 288–291 (IEEE, 2013).
81. Jerath, K., Brennan, S. & Lagoa, C. Bridging the gap between sensor noise modeling and sensor characterization. *Measurement* **116**, 350–366 (2018).
82. Mackowiak, V., Peupelmann, J., Ma, Y. & Gorges, A. *NEP–Noise Equivalent Power* (Thorlabs, Inc, 2015).
83. Jerry, M., Shukla, N., Paik, H., Schlom, D. G. & Datta, S. Dynamics of electrically driven sub-nanosecond switching in vanadium dioxide. In *Proc 2016 IEEE Silicon Nanoelectronics Workshop (SNW)*, Honolulu, HI, USA, 26–27 (IEEE, 2016).
84. Qaderi, F. et al. Subthreshold VO_2 vertical switches for large-bandwidth millimeter-wave and sub-terahertz detection. In *Proc 2022 47th International Conference on Infrared, Millimeter and Terahertz Waves (IRMMW-THz)*, Delft, Netherlands, 1–2 (IEEE, 2022).
85. Madan, H., Jerry, M., Pogrebnyakov, A., Mayer, T. & Datta, S. Quantitative mapping of phase coexistence in mott-peierls insulator during electronic and thermally driven phase transition. *ACS Nano* **9**, 2009–2017 (2015).
86. Lee, D. et al. Isostructural metal-insulator transition in VO2. *Science* **362**, 1037–1040 (2018).
87. Jian, J. et al. Roles of grain boundaries on the semiconductor to metal phase transition of VO2 thin films. *Appl. Phys. Lett.* **107**, 102105 (2015).
88. Davids, P. S. et al. Infrared rectification in a nanoantenna-coupled metal-oxide-semiconductor tunnel diode. *Nat. Nanotechnol.* **10**, 1033–1038 (2015).
89. Sharma, A., Singh, V., Bougher, T. L. & Cola, B. A. A carbon nanotube optical rectenna. *Nat. Nanotechnol.* **10**, 1027–1032 (2015).

Acknowledgements

This project has been funded by the European Research Council (ERC) via the Advanced ERC Grant Millitech, having as Principal Investigator professor Mihai Adrian Ionescu. The funder is the European Commission, grant agreement 695459.

Author contributions

A.M.I. and F.Q. developed the device principle. F.Q. optimized the VO_2 thin film deposition recipe and fabricated the devices. F.Q. conducted static measurements on the sensor. F.Q. and T.R. worked on the oscillator circuit experiment. D.F. analyzed the bimodal distributions and the Allan deviation. F.Q., M.B. and J.L. conducted the high-frequency measurements. F.Q. and A.M.I. wrote the manuscript.

Competing interests

The authors declare no competing interests.

Additional information

Supplementary information The online version contains supplementary material available at https://doi.org/10.1038/s43246-023-00350-x.

Correspondence and requests for materials should be addressed to Fatemeh Qaderi or Adrian M. Ionescu.

Peer review information *Communications Materials* thanks Shihab Al-Daffaie and the other, anonymous, reviewer(s) for their contribution to the peer review of this work. Primary Handling Editors: Klaas-Jan Tielrooij and Aldo Isidori. Peer reviewer reports are available.

Reprints and permission information is available at http://www.nature.com/reprints

Publisher's note Springer Nature remains neutral with regard to jurisdictional claims in published maps and institutional affiliations.

Open Access This article is licensed under a Creative Commons Attribution 4.0 International License, which permits use, sharing, adaptation, distribution and reproduction in any medium or format, as long as you give appropriate credit to the original author(s) and the source, provide a link to the Creative Commons license, and indicate if changes were made. The images or other third party material in this article are included in the article's Creative Commons license, unless indicated otherwise in a credit line to the material. If material is not included in the article's Creative Commons license and your intended use is not permitted by statutory regulation or exceeds the permitted use, you will need to obtain permission directly from the copyright holder. To view a copy of this license, visit http://creativecommons.org/licenses/by/4.0/.

© The Author(s) 2023